



Article

Influence of the Cooling Rate on Austenite Ordering and Martensite Transformation in a Non-Stoichiometric Alloy Based on Ni-Mn-In

Dmitriy Kuznetsov ^{1,*} , Elena Kuznetsova ², Alexey Mashirov ¹ , Denis Danilov ³ , Georgiy Shandryuk ⁴, Irek Musabirov ⁵ , Igor Shchetinin ⁶, Alexey Prokunin ¹ , Svetlana von Gratowski ¹ and Vladimir Shavrov ¹

- ¹ Kotelnikov Institute of Radioengineering and Electronics of Russian Academy of Sciences, 125009 Moscow, Russia; a.v.mashirov@mail.ru (A.M.); prokunin.av@phystech.edu (A.P.); svetlana.gratowski@yandex.ru (S.v.G.); shavrov@cplire.ru (V.S.)
- ² M.N. Mikheev Institute of Metal Physics of Ural Branch of Russian Academy of Sciences, 620108 Ekaterinburg, Russia; eik3108@yandex.ru
- ³ IRC for Nanotechnology of the Science Park of St. Petersburg State University, 199034 St. Petersburg, Russia; d.danilov@spbu.ru
- ⁴ A.V. Topchiev Institute of Petrochemical Synthesis of Russian Academy of Sciences, 119991 Moscow, Russia; gosha@ips.ac.ru
- ⁵ Institute for Metals Superplasticity Problems of Russian Academy of Sciences, 450001 Ufa, Russia; irekmusabirov@imsp.ru
- ⁶ Department of Physical Materials Science, National University of Science and Technology MISIS, 119049 Moscow, Russia; ingvar@misis.ru
- * Correspondence: kuznetsov.dmitry89@gmail.com



Citation: Kuznetsov, D.; Kuznetsova, E.; Mashirov, A.; Danilov, D.; Shandryuk, G.; Musabirov, I.; Shchetinin, I.; Prokunin, A.; von Gratowski, S.; Shavrov, V. Influence of the Cooling Rate on Austenite Ordering and Martensite Transformation in a Non-Stoichiometric Alloy Based on Ni-Mn-In. *J. Compos. Sci.* **2023**, *7*, 514. <https://doi.org/10.3390/jcs7120514>

Academic Editors: Salvatore Brischetto

Received: 25 October 2023
Revised: 14 November 2023
Accepted: 6 December 2023
Published: 11 December 2023



Copyright: © 2023 by the authors. Licensee MDPI, Basel, Switzerland. This article is an open access article distributed under the terms and conditions of the Creative Commons Attribution (CC BY) license (<https://creativecommons.org/licenses/by/4.0/>).

Abstract: The effect of the melt cooling rate on the atomic ordering of austenite and, as a consequence, on the martensitic transformation of a nonstoichiometric alloy of the Ni-Mn-In system has been studied. In situ TEM observations revealed differences in the mechanism of phase transformations of the alloy subjected to different cooling conditions. It is shown that during quenching a high density of antiphase boundaries (APB) is formed and the alloy is in the austenite–martensitic (10M and 14M) state up to a temperature of 120 K. In a slowly cooled alloy, a lower APB density is observed, and a two-stage transformation, $L2_1/B2 \rightarrow 10M \rightarrow 14M$, occurs in the range of 150–120 K.

Keywords: austenite; ordering; martensitic transformation; Ni-Mn-In; in situ TEM; decomposition

1. Introduction

Interest in Ni-Mn-In alloys is mainly focused on non-stoichiometric compositions, especially on the manganese-enriched Ni₂Mn(In, Mn) system. Studies have shown that the structure of unmodulated martensite exists in alloys with a relatively low In content ($x \leq 10$) [1]. With an increase in the content of In ($10 < x \leq 16$), the crystal structure of martensite has a long-period layered-modulated structure and is characterized by good magnetically sensitive characteristics. In alloys based on Ni-Mn-In, modulated structures 6 M, 5 M and 7 M were observed [2,3]. Therefore, the accurate determination of the crystal structure of austenite and martensite is of key importance for controlling the effects associated with martensitic transformations, such as magnetic memory (MM), the shape memory effect (SME), and the magnetocaloric effect (MCE).

When cooled from the melt, alloys with the Heusler (for example X_2YZ , XY_2Z , and other) structure can undergo a series of disorder–order transitions, $A2 \rightarrow B2 \rightarrow L2_1$ ($D0_3$, $C1_b$, and some others), depending on the occupancy of positions between the X, Y, and Z sublattices [4]. Alloys based on the Ni-Mn-In system of a non-stoichiometric composition are prone to decay into an energetically favorable structure with a 2-1-1 stoichiometry and the rest of the alloy, which forms various structures with different compositions [5]. Depending on the degree of atomic ordering, it is assumed that the Ni-Mn-In compound

will contain structural domains and APB formed during the transition from the partially ordered B2 phase to the ordered L2₁. Therefore, the structural order of the austenitic phases depends on the conditions and cooling rate. The papers [6,7] describe methods for the formation of APB in Heusler alloys. In the case of a quenched sample, APBs are formed as a result of a thermally induced order–disorder transition [7]. Or, in the case of slow cooling with a furnace, APBs mainly develop due to the merging of two neighboring L2₁ ordered regions [6].

In [8], the relationship between APB, the structure of magnetic domains, and the functional properties of Ni-Mn-Ga single crystals was studied. The APB density was controlled using various thermal treatments, and the magnetic domains were observed using Lorentz transmission electron microscopy. Slow cooling resulted in low density, air quenching to medium density, and water quenching to high APB density. The pinning of the walls of the magnetic domains on the APB was observed, which led to a one-to-one correspondence between the magnetic domain walls and the APB.

In this work, the influence of the cooling rate on the atomic ordering of the austenitic phase of the Ni-Mn-In system inherited by the martensite structure and, accordingly, on the nature of the martensitic transformation was studied.

In-depth investigations into the intricate structure of non-stoichiometric alloys and decomposition processes are seldom documented, with only a handful of mentions in a recent review [9], including a contribution from this paper's authors. The focus has primarily been on the crystal structure of stoichiometric alloys [10]. As such, a systematic exploration of microstructure evolution during the cooling process is warranted. Numerous studies have examined the property dependence of Heusler alloys on composition [9–18], but this perspective is incomplete. Our research reveals how material properties are influenced by structural characteristics for identical compositions. This paper demonstrates that inconsistencies in reported martensite structures in the studied system could be linked to decomposition and variations in the ratio of anti-phase boundaries in austenite. Consequently, it is postulated that the actual martensite structure is contingent on the specifics of the preceding austenite state and the conditions under which martensite is formed. By integrating findings from TEM examinations with calorimetric characteristics and X-ray diffraction, we have gained a more precise understanding of the microstructure's role in the magnetostructural transformation of this shape memory alloy system, magnetic memory, and caloric effects, and have identified strategies for enhancing functional properties.

2. Experimental Technique and Methods

Polycrystalline samples of the Ni-Mn-In alloy in the form of ingots weighing about 30 g were made from high-purity initial metals, namely Ni, Mn, and In (99.99%), via arc melting in an argon atmosphere on a cold hearth with three flips and remelting. For the purpose of homogenization, the ingots were annealed in vacuum at a temperature of 1173 K for 48 h. The ingots were cooled in two ways: natural (slow) cooling in a furnace to room temperature and rapid cooling into water at a temperature of 288 K (quenching). Alloy cooled naturally with a furnace to room temperature of 300 K, and an average cooling rate calculated as $(1173\text{ K} - 300\text{ K})/437\text{ min} = 1.997\text{ K/min}$. For an alloy quenched in water at a temperature of 288 K, the quantitative assessment of the cooling rate is quite difficult; however, the purpose of quenching was to suppress diffusion processes, namely, the decomposition of the solid solution, and the certification of various areas of the quenched sample using the TEM and SEM methods showed that the structure inside the ingot and its surface is the same in these areas. X-ray diffraction data confirmed this. Thus, the purpose of hardening has been achieved—the sample is completely hardened. The surface of the hardened sample reached the water temperature, that is, 288 K, in about 10 s, it can be assumed that the temperature of the entire ingot leveled out in about 15–20 s, in which case the average cooling rate is between 44 and 60 K/s.

The nominal composition was Ni₄₆Mn₄₁In₁₃ ($e/a = 7.86$), which coincided with the average data of energy dispersive spectroscopy (EDX) over the diameter of the spherical

ingot. The elemental analysis of the foil was also determined via the EDX method in TEM with an error of less than 1 at. % and resulted in $\text{Ni}_{44.9}\text{Mn}_{39.9}\text{In}_{15.2}$ ($e/a = 7.73$) for quenched samples and $\text{Ni}_{45.6}\text{Mn}_{39.5}\text{In}_{14.9}$ ($e/a = 7.77$) for slowly cooled samples. Within the margin of error of the EDX, no noticeable signs of oxygen were detected.

The microstructure of the samples was studied in the temperature range 120–300 K using a Carl Zeiss Libra 200FE transmission electron microscope (TEM) (accelerating voltage 200 kV) (Oberkochen, Germany) with an OMEGA energy filter, an Oxford Instruments (Abingdon, UK) X-Max 80 energy-dispersive X-ray detector, and a Gatan (Pleasanton, CA, USA) Model 636 two-axis cryoanalytical holder with a Model 900 SmartSet cold stage controller. Foils for TEM were obtained via mechanical thinning with abrasives of various fineness (1000, 1500, 2000 CW) up to sample thickness 200 μm , and further thinning was carried out electrochemically in an ethanol solution of 30% nitric acid at room temperature with a voltage of 18–20 V. The final thinning was carried out in an ion polishing unit with argon ions, accelerating voltages from 4 to 1 keV, with a step of 1 keV, and a polishing time of 10 min for each step, and the current dropped from 20 μA at 4 keV to 1.5 μA at 1 keV. Electron microscopy studies and foils preparation for TEM were carried out at the IRC Nanotechnology, Science Park, St. Petersburg State University, 199034, St. Petersburg, Russia.

The characteristic temperatures of the beginning and end of the forward and reverse thermoelastic metamagnetostructural (hereafter, for simplicity, martensitic) transformations and the Curie temperature were determined via differential scanning calorimetry (DSC) on a METTLER TOLEDO DSC3+ setup in the temperature range from 100 to 600 K at a speed of 2 K/min and via the thermogravimetric (TGA) method, respectively. The method of thermomechanical analysis (TMA) determined changes in the linear dimensions of the sample as a result of martensitic transformation and thermal expansion coefficients (TEC).

X-ray diffraction studies in the temperature range from 86 K to 573 K were carried out on a Rigaku Ultima IV multifunctional diffractometer using $\text{CuK}\alpha$ radiation, a graphite monochromator on a diffracted beam of a scintillation detector, and a low- and medium-temperature attachment LMT (Rigaku, Japan, Tokyo).

3. Results Discussion

Thermal analysis determined the martensitic transformation temperatures; DSC data are presented in Figure 1. Quenching led to an increase in the temperature of direct and reverse martensitic transformations but did not affect the width of the hysteresis. The thermogram shows that hardening leads to a decrease in the Curie temperature and “brings together” the phase transformations of the first and second order, that is, the martensitic transformation and the Curie point, compared to a slowly cooled alloy. Moreover, the latent heat of the martensitic phase transformation in a slowly cooled alloy is approximately equal to that for the Curie point and is much less than that for the martensitic transformation of a quenched alloy. From this, it should be expected that the magnetocaloric effect for the quenched alloy as a result of martensitic transformation will be higher. For both alloys, the peaks on the thermogram are not sharp, and the martensitic transformation occurs in a wide temperature range (on the order of 20–25 K), gradually approaching the Curie point.

Table 1 presents the characteristic temperatures of direct martensitic (M_s and M_f) and reverse martensitic (A_s and A_f) transformations, which were determined using the secant method (Figure 1).

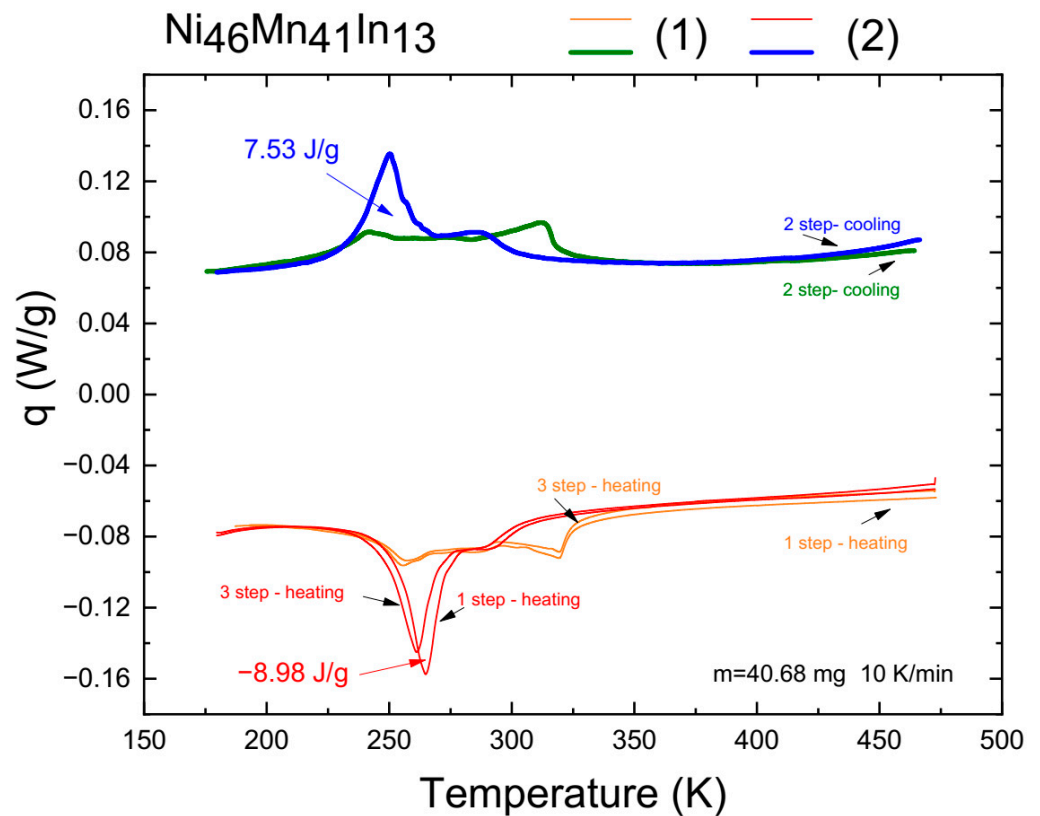


Figure 1. DSC data for (1) slowly cooled and (2) quenched alloys.

Table 1. Characteristic temperatures of Ni₄₆Mn₄₁In₁₃ alloys both slowly cooled and quenched.

Heat Treatment \ Temperatures of Phase Transformations, K	As1	Af1	Ms	Mf	As2	Af2
Quenched	274	252	263	234	270	247
Slowly cooled	267	246	252	227	267	246

Thermogravimetric analysis specified the Curie temperature, and it was 321 K for the slowly cooled sample and 305 K for the quenched sample, see Figure 2.

The temperature dependences of the magnetizations of a quenched microsample weighing 1.51 mg in magnetic fields of 0.018, 1, 3, and 5 T are presented in Figure 3. The metamagnetic structural phase transition is highly diffuse and does not complete until 170 K. The shift in the characteristic temperature Ms during magnetization is 4 K/T. It can be seen that with decreasing sample size, the temperature region of existence of the metamagnetostructural phase transition increases from the range of approximately 274–234 K to 291–167 K (Table 1). Similar behavior is observed in thin films with a thickness of 50–150 nm. An increase in the proportion of surface energy relative to volumetric energy is qualitatively similar to stress fields that expand the region of existence of ferromagnetic austenite and thereby lower the temperature Mf to 160 K. For the slowly cooled alloy see [5].

Thermomechanical analysis shows a linear change in CTE outside the region of martensitic transformations and a sharp jump as a result of martensitic transformation, and hysteresis is also observed. In this case, the CTE of the hardened sample as a result of martensitic transformation is almost two times higher (Figure 4).

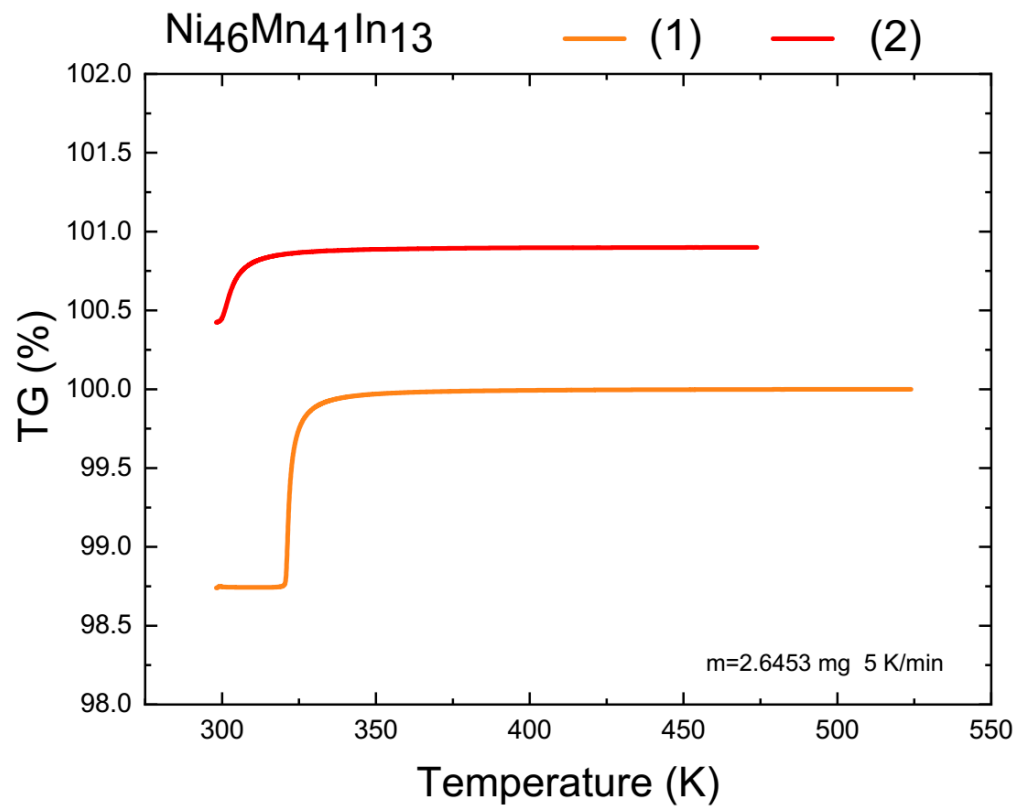


Figure 2. TGA data for slowly cooled (1) and quenched (2) alloys.

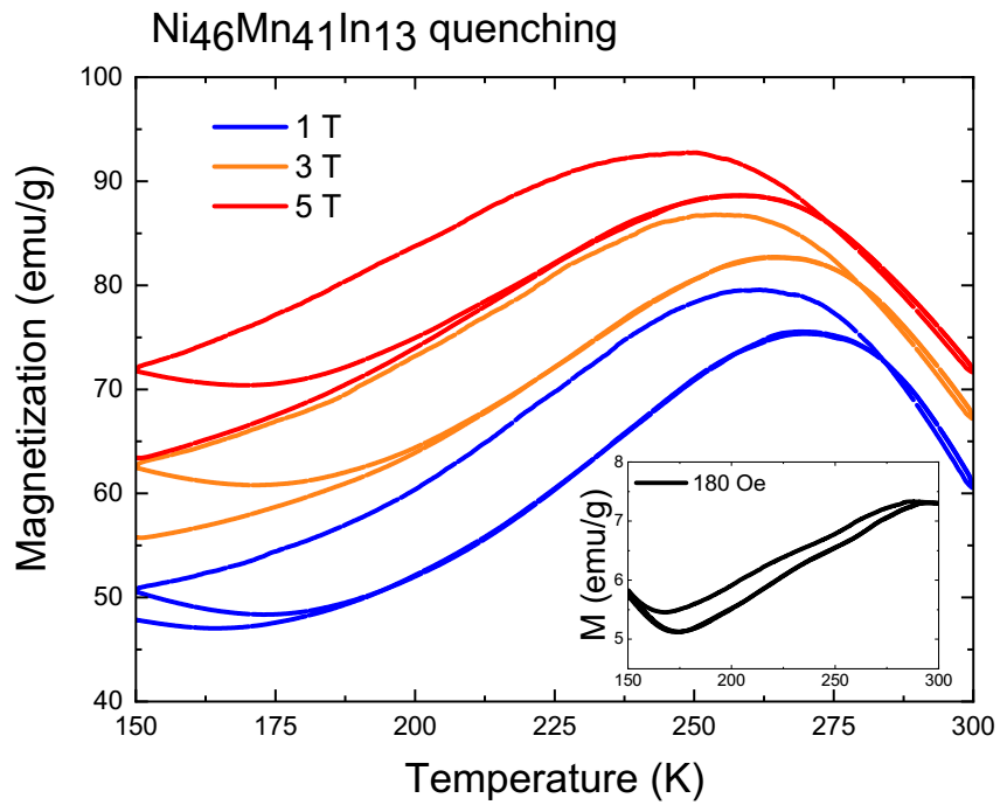


Figure 3. Temperature dependence of the magnetization of a quenched micro-sized sample in magnetic fields of 0.018, 1, 3, and 5 T.

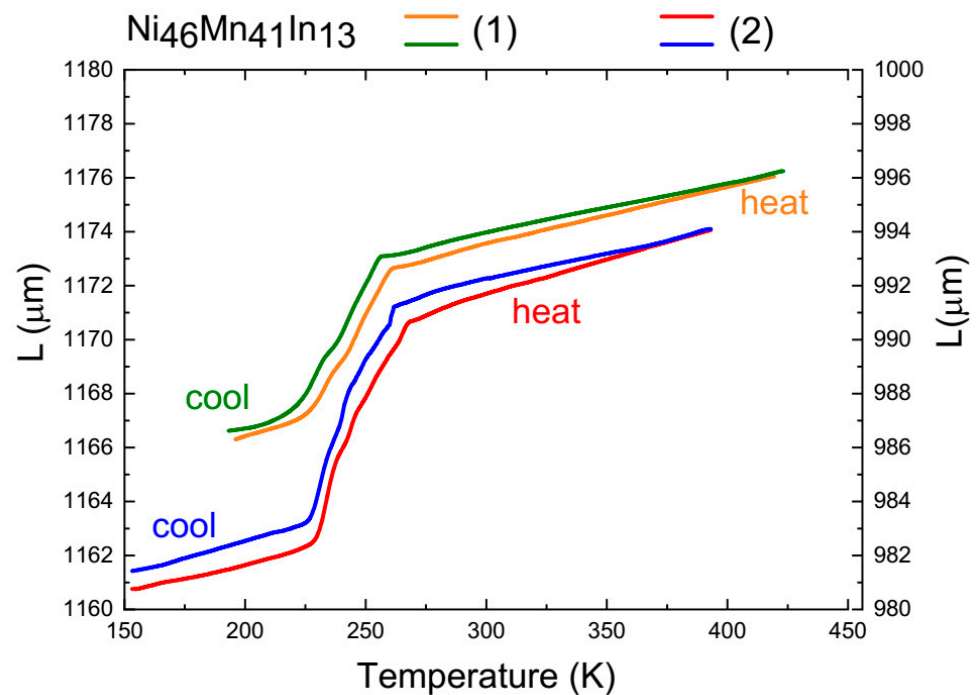


Figure 4. TMA data for slowly cooled (1) and quenched (2) alloys.

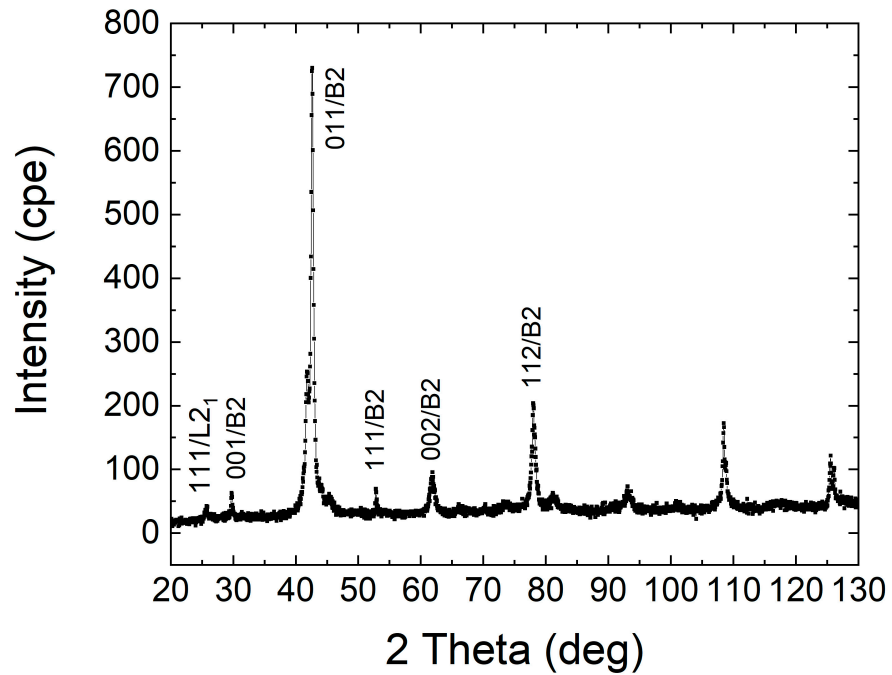
Figure 5 shows X-ray patterns of quenched (a, b) and slowly cooled (c, d) alloys being studied. The space group of the crystal lattices of both alloys is $Fm\bar{3}m$. At room temperature, both alloys are in the austenitic state with bcc fundamental lattice reflections (220), (400), and (422) of the highly ordered phase $L2_1$. Since the $B2 \rightarrow L2_1$ ordering process is a diffusion process, predominantly proceeding at maximum rates at temperatures of 0.6–0.9 of the melting point, a slowly cooled sample should have a large fraction $L2_1$ of the ordered solid solution. Indeed, superstructural reflections (111), (311), and (331) in a slowly cooled alloy indicate that a part of the austenite is ordered according to the $L2_1$ type. The well-pronounced peak (111) in the X-ray diffraction pattern of the slowly cooled sample indicates a higher proportion of $L2_1$ than that of the quenched sample, in which the (200) $L2_1$ /(001) $B2$ peak is better pronounced, and the (311) and (331) reflections are practically absent.

After cooling to 86 K, the (220) peak of the austenitic high-temperature phase disappears in both samples, and a martensitic microstructure appears in the alloys, in which the austenite peaks become very weak (in a slowly cooled alloy, they practically disappear). However, the crystal structures of these martensites are different. In [19,20], the parameters of the crystal lattice of 14 M martensite in the $Ni_{47}Mn_{42}In_{11}$ alloy during cooling were determined using the lattice periods and angles measured using the X-ray method, and the profile of the X-ray peaks of Bragg reflections in the 2θ angles for a martensite crystal was calculated. Using these data, it is possible to index the X-ray diffraction pattern of the slowly cooled alloy as 14 M martensite with a monoclinic structure. The X-ray diffraction pattern of the hardened alloy, taken at 86 K, shows a complex two-phase structure of cubic austenite and modulated martensite. Apart from reflections from austenite and martensite, no additional peaks are observed.

At 300 K, a tweed-banded diffraction contrast was observed in bright-field images of the austenite of the quenched Ni-Mn-In alloy (Figure 6a). Tweed contrast is accompanied by the appearance of satellites and/or diffuse scattering in diffraction patterns (Figure 6b). The main diffraction spots (all diffraction patterns are indexed according to $L2_1$ ordering) belong to a cubic cell with a lattice parameter $a = 5.99 \text{ \AA}$. Since the $L2_1$ phase is an ordered Heusler phase, it can be unambiguously identified in microdiffraction patterns only with the [110] zone axis due to characteristic superlattice reflections of the [111] type, knowing

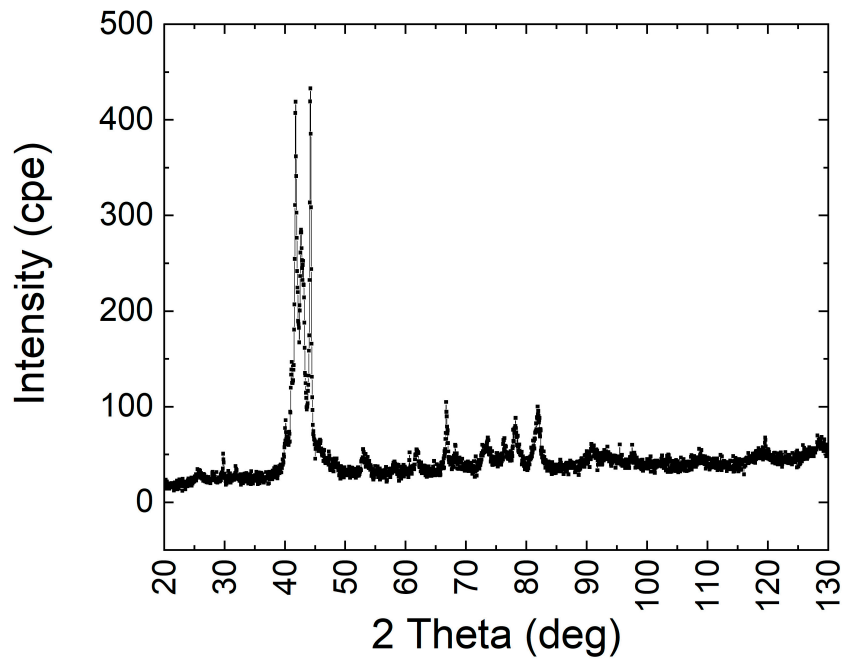
what type of austenite phase is ordered ($L2_1$ or B2) according to diffraction patterns is impossible, but, as indicated above, X-ray diffraction established the presence of a phase ordered according to the $L2_1$ type. In the dark-field images shown in Figure 6c–e, the [220] type reflections show a contrast from APBs, which are flat defects inherent only in ordered alloys, i.e., quenching did not completely suppress the $B2 \rightarrow L2_1$ ordering process.

Ni₄₆Mn₄₁In₁₃ (quench) CuK α , 300 K



(a)

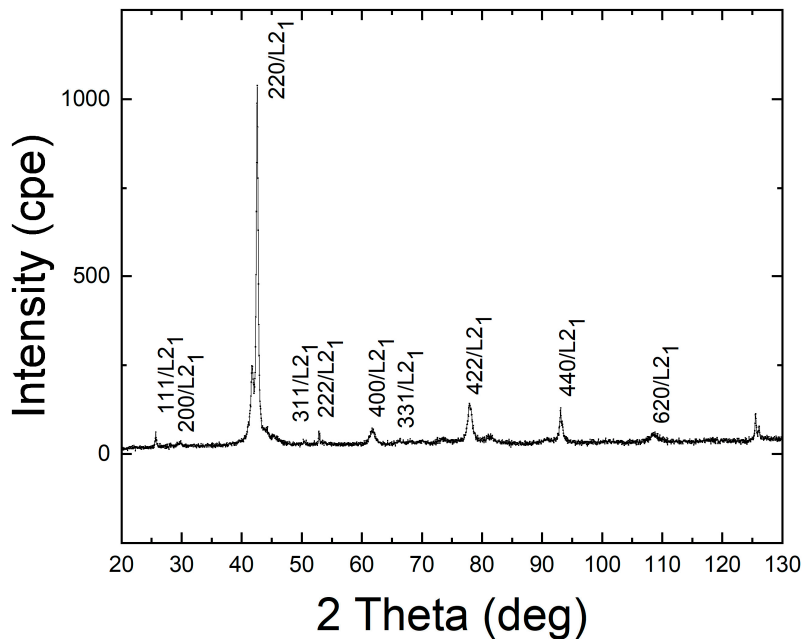
Ni₄₆Mn₄₁In₁₃ (quench) CuK α , 86 K



(b)

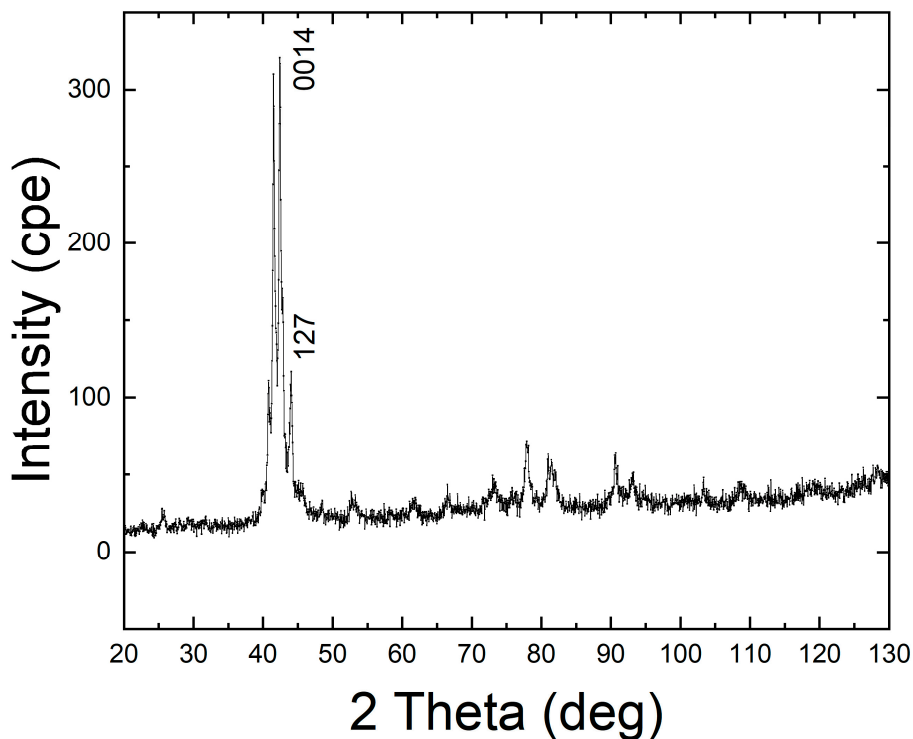
Figure 5. Cont.

Ni₄₆Mn₄₁In₁₃ (slowly cooled) CuKα, 300 K



(c)

Ni₄₆Mn₄₁In₁₃ (slowly cooled) CuKα, 86 K



(d)

Figure 5. X-ray diffraction patterns of quenched (a,b) and slowly cooled (c,d) alloys.

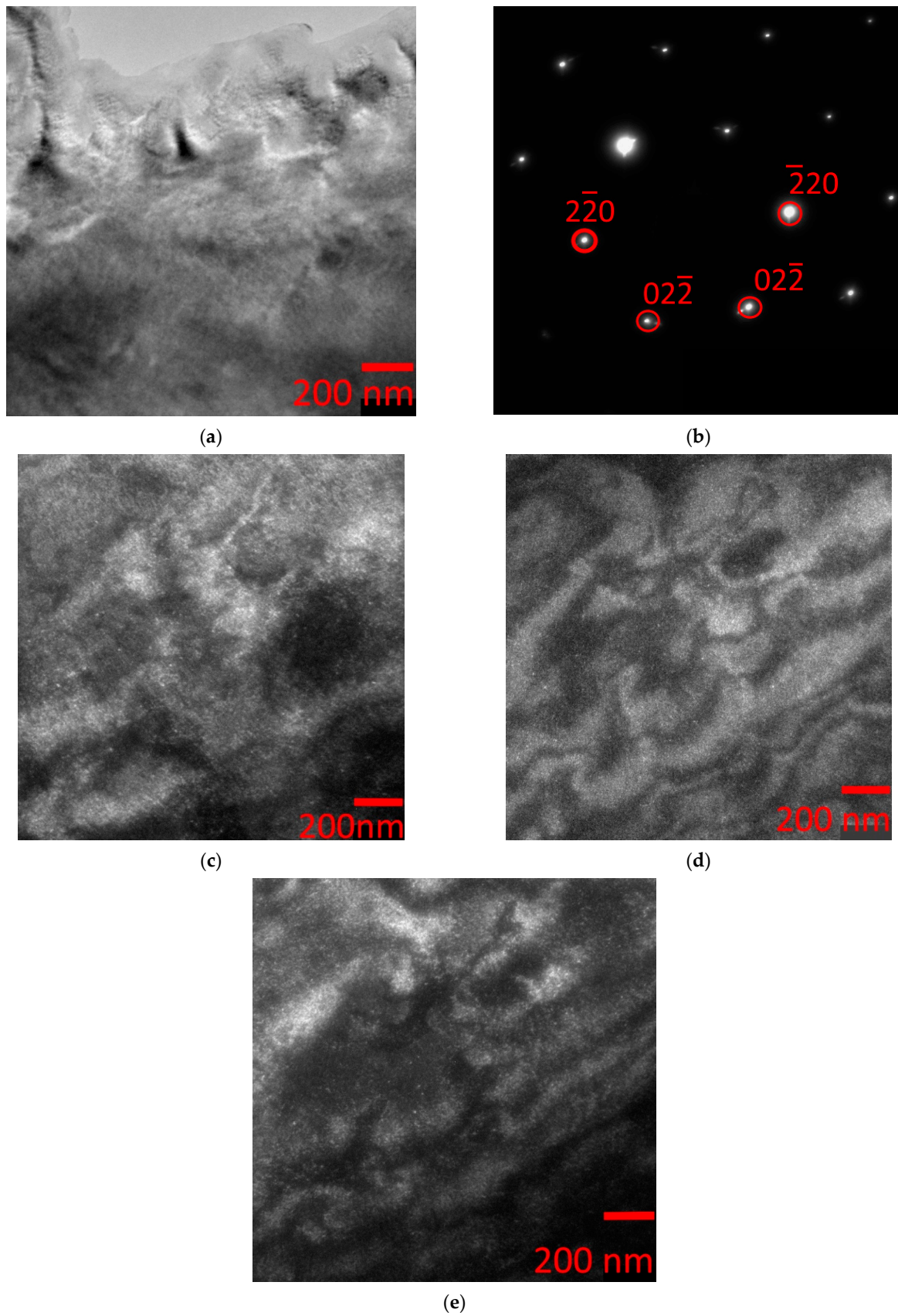


Figure 6. Bright-field TEM image (a), with the corresponding microelectron diffraction pattern with the zone axis $[111]L_2$ (b) and dark-field TEM images in structural reflections 02-2 (c), 20-2 (d), and 2-20 (e) of quenched austenite alloy $Ni_{45}Mn_{43}In_{12}$. Observations at 300 K.

At temperatures of 120–160 K, the quenched alloy is in a two-phase austenite–martensite state (Figure 7). Figure 7a shows a TEM image taken at 160 K and illustrates, at first glance, the appearance of acicular martensite. In the bright-field image at a higher magnification (Figure 7b), two regions marked I and II can be distinguished, the diffraction patterns of which are shown in Figure 7c and 7d, respectively. The diffraction pattern obtained from region I (Figure 7c) shows diffuse strands between the main reflections and extra reflections at positions $1/5\langle 220 \rangle * L_{21}$ along the $\langle 110 \rangle * L_{21}$ directions (indicated by arrows). Extra reflections of this type suggest the formation of a modulated 10 M martensite structure. But instead of twins, region I is characterized by a tweed contrast due to the formation of a nanodomain structure consisting of retained austenite and martensite ($L_{21}/B2 + 10 M$) or the observed structure corresponds to a pre-martensitic state, since there are diffuse scattering effects characteristic of such a state along the $\langle 110 \rangle$ directions on diffraction picture. In region II, a contrast is observed in the form of a system of bands, which can be correlated with the pre-martensitic state to the fine-twin structure of the long-period 14 M martensite. One of the systems of bands is perpendicular to the direction of splitting of the main reflections when satellites appear and is parallel to one of the families of planes of the $\{110\}L_{21}$ type. The distant reflections have extra reflections in positions $1/7\langle 220 \rangle * L_{21}$ (Figure 7d, indicated by arrows), which suggests the formation of a modulated 14 M structure. In addition, the absence of twinning may be due to the fact that the martensitic transition is observed at a very early pre-martensitic stage, when the appearance of twins as a stress relief mechanism has not yet arisen. Thus, the analysis of diffraction patterns at temperatures of 120–160 K shows a pre-martensitic nanodomain austenite–martensitic (10 M and 14 M) state. Dark-field images (Figure 8) show that in the main structural reflections belonging to the austenite phase and in the electron diffraction pattern from region I of the coexistence of austenite with 10 M martensite (Figure 8b,c), high-density APBs burn. These regions are interspersed with plates of II coexistence of austenite with 14 M martensite (Figure 8d), which burn in extra reflections corresponding to 14 M martensite (extra reflections are circled in the electron diffraction pattern in Figure 7d). The dark-field image reveals a fine streaky structure on plate II. The projection directions of the normal to the thin banded contrast are parallel to the splitting direction of the $\langle 220 \rangle * L_{21}$ reflections in the microdiffraction patterns.

On dark-field images, the interface between plates I and II looks interesting, clean, and even. The thickness of this region, when plate I shines, is ~ 100 nm, and when plate II shines, the thickness is almost three times less. Moreover, the regions overlap in dark-field images, that is, the diffraction effects related to the structure of the region belonging to both plate I and plate II.

The slowly cooled alloy at room temperature has a cubic crystal lattice of austenite ordered according to the $L_{21}/B2$ type. A tweed contrast is observed on the bright and dark field TEM images of the austenite structure of the alloy under study (Figure 9a). At slow cooling rates from the melt, the nonstoichiometric Ni-Mn-In alloy can decompose into regions that differ both in chemical composition and in different levels of ordering, which leads to the formation of a modulated periodic austenite structure [5]. The dark-field image (Figure 9b) obtained in the 02–2 reflection (all diffraction patterns are also indexed according to the L_{21} ordering) shows a contrast from APBs in which the L_{21} superstructure is broken and the order of atoms is close to the B2 structure. The size of the L_{21} domains observed in the bright and dark field images is ~ 150 nm, i.e., much larger than in the case of the quenched alloy. Along with an increase in the domain size, the volume fraction of APB becomes smaller, which suggests that the kinetics of martensitic transformation can change with the density of APB.

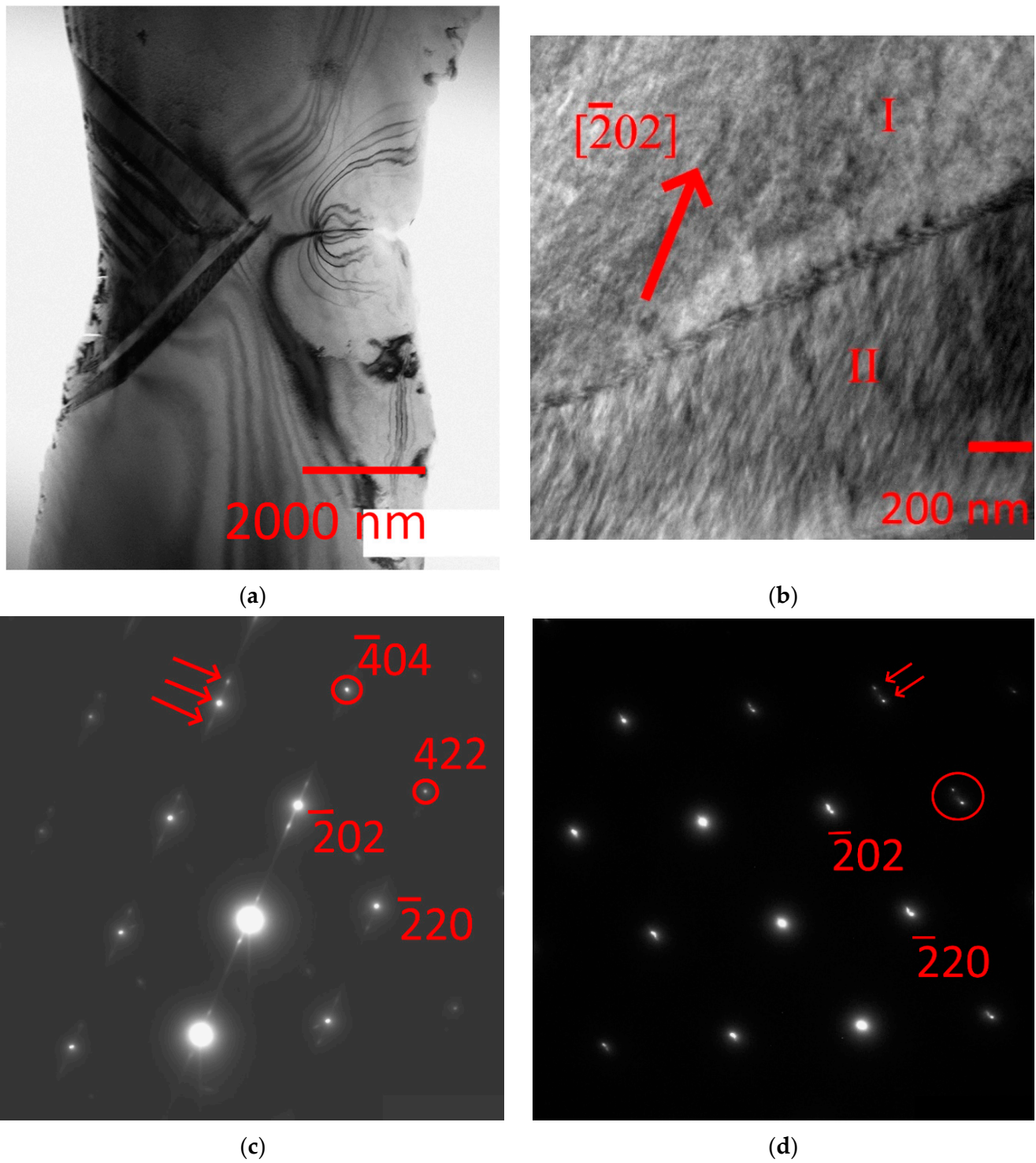


Figure 7. Microstructure of the quenched $\text{Ni}_{45}\text{Mn}_{43}\text{In}_{12}$ alloy: (a,b) bright-field images at 160 K and 120 K; (c,d) electron diffraction patterns with the $[111]_{\text{L21}}$ zone axis from zones I and II, respectively.

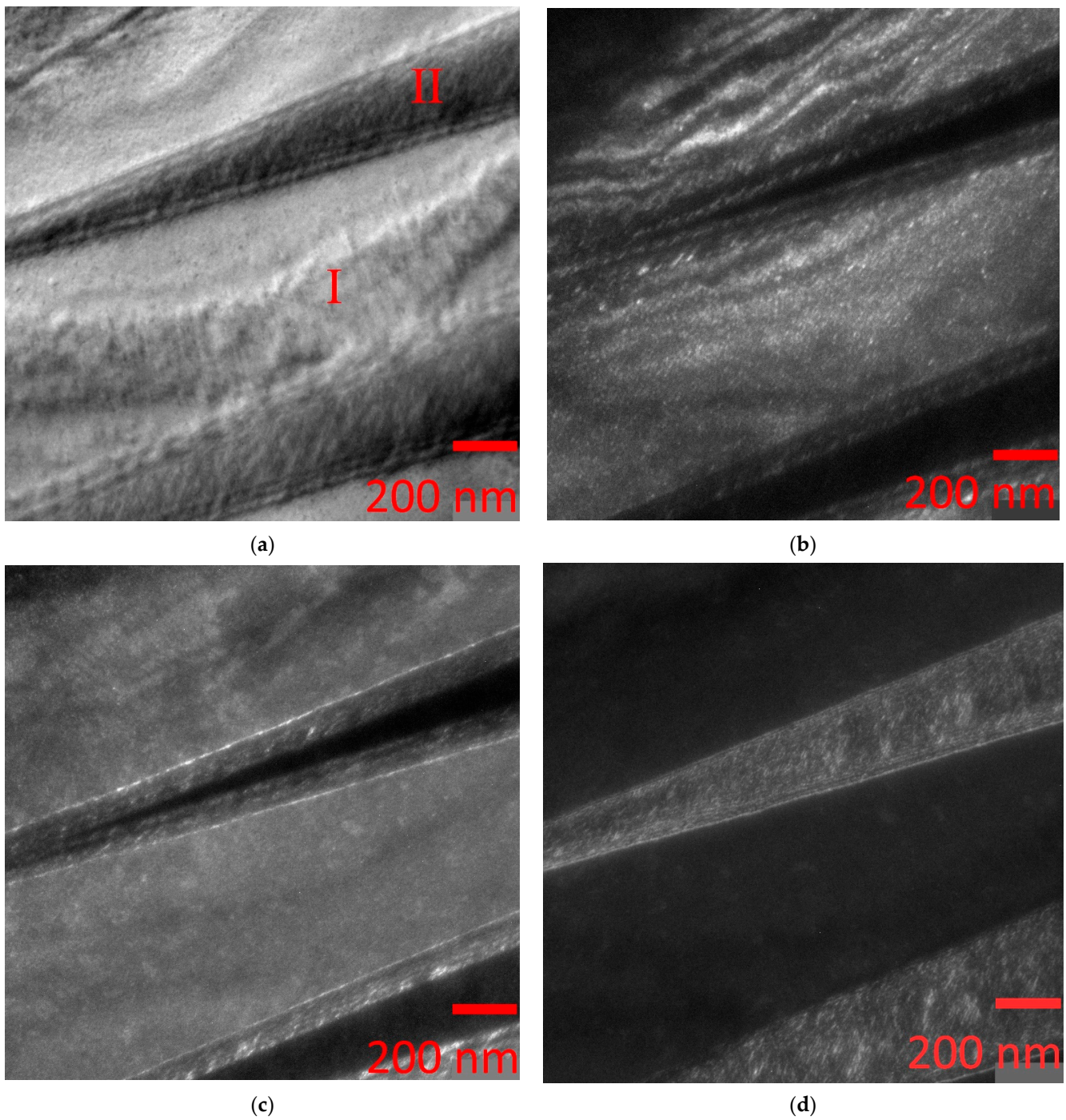


Figure 8. Microstructure of the quenched $\text{Ni}_{45}\text{Mn}_{43}\text{In}_{12}$ alloy: (a) bright-field image at 120 K; (b,c) dark-field images in reflections -404 and -422 indicated by circles in the electron diffraction pattern in Figure 6c; (d) dark-field image in the double reflection shown in the electron diffraction pattern in Figure 6d.

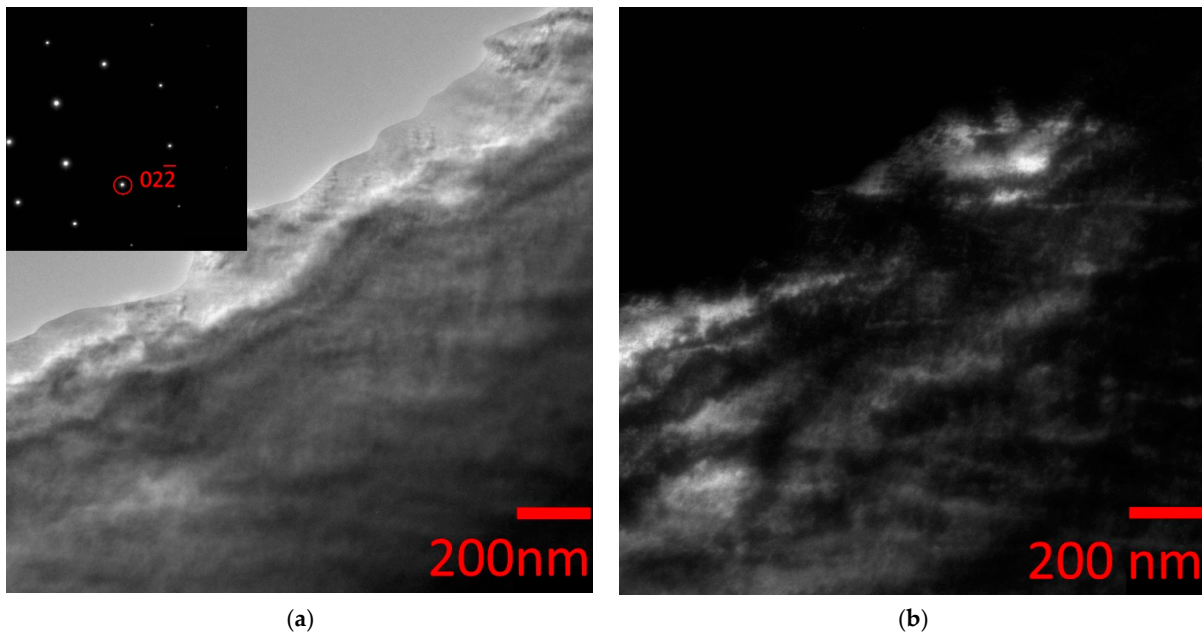


Figure 9. Bright-field (a) and dark-field TEM images of austenite in the slowly cooled $\text{Ni}_{45}\text{Mn}_{40}\text{In}_{15}$ alloy in the 02-2 structural reflection (b); in the inset, an electron diffraction pattern with the $[111]L_2$ zone axis. Observations at 300 K.

In situ cooling experiments have shown the sequence of martensite formation. In a slowly cooled alloy, when the temperature drops to 150 K, the martensitic transformation proceeds with the formation of modulated martensite 10 M ($L_2/B_2 \rightarrow 10\text{ M}$). On Figure 10a is a bright field image showing the microstructure within a martensite plate (in the center of the figure). The corresponding diffraction pattern (Figure 10b) shows superstructural reflections typical of 10 M martensite when two main spots are separated by four satellite spots. The fine structure of the 10 M martensitic region becomes visible as a result of the visualization of the contrast from many parallel stacking faults, which is a kind of additional shear to accommodate the transformation and achieve the formation of an invariant plane between austenite and martensite. The diffuse character of superstructural reflections also indicates a high stacking fault density.

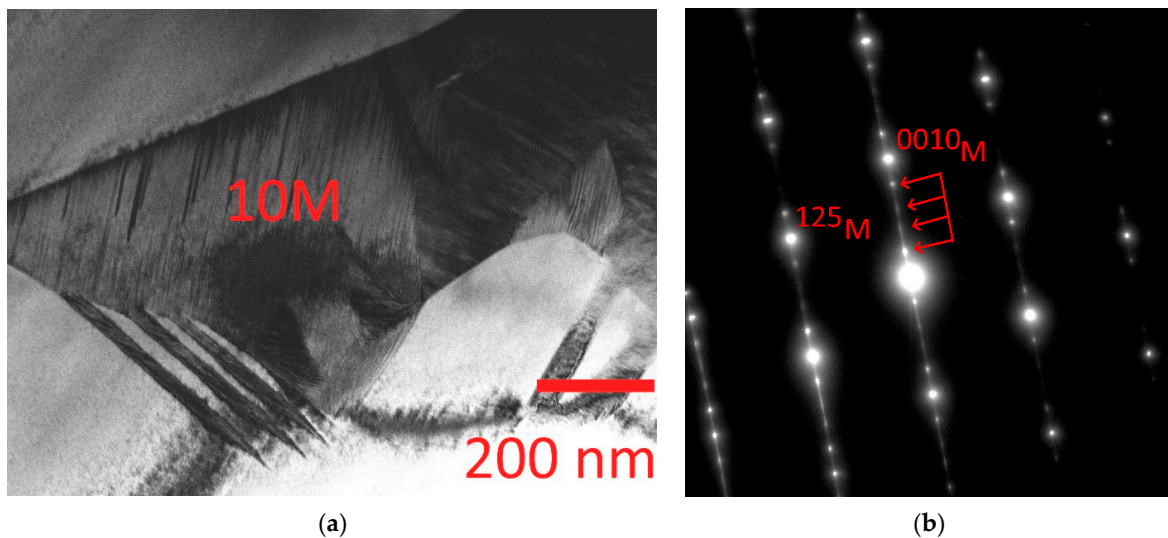


Figure 10. Microstructure of slowly cooled $\text{Ni}_{45}\text{Mn}_{40}\text{In}_{15}$ alloy: (a) bright-field image at 150 K; (b) electron diffraction pattern with the $[111]L_2$ zone axis from the 10 M region.

An analysis of the diffraction patterns obtained from a thin foil at 120 K revealed various structures. It is possible to single out at least three different structural-phase regions shown in Figure 11 along with the corresponding diffraction patterns. The simultaneous appearance of various structures in thin films or foils in comparison with the bulk structure is a phenomenon associated with the fact that the martensitic transformation strongly depends on size effects, i.e., on the ratio of volume and surface energies, and is completely suppressed when the plate thickness is less than 50 nm [21]. In the area of Figure 11 (in the thin part, right circle), there is a tweed contrast with characteristic diffuse scattering in the diffraction pattern in the form of diffuse strands (L_{21}/B_2). The region to the left (center circle) contains a mixture of cubic austenite and 14 M martensite ($L_{21}/B_2 + 14 M$). In the leftmost region deep in the foil (in the thickest part, left circle), a multilayer 14 M martensite is formed, the orientation relationships between the high-temperature L_{21} phase and 14 M martensite are: $(001)14 M \parallel (110)L_{21}$. Lowering the in situ temperature of the slowly cooled alloy to 120 K caused the 10 M martensite regions to undergo a martensitic transformation to 14 M martensite. Microdiffraction patterns obtained from 14 M martensite (Figure 12) contain rows of extra reflections of the $1/7\langle 220 \rangle^*$ type along the $\langle 110 \rangle^*L_{21}$ directions. The dark-field image (Figure 12c), taken in two extra reflections of the 14 M crystal (marked with a circle in Figure 12b), shows a thin banded structure inside the plates, which is not revealed in the bright-field image. The projection directions of the normal to the thin banded contrast are parallel to the $[0014]M$ direction in the microdiffraction pattern. Thus, an initially single-phase alloy at room temperature, ordered according to the L_{21}/B_2 type, experiences a two-stage austenite–martensite–martensite transformation $L_{21}/B_2 \rightarrow 10 M \rightarrow 14 M$, since its microdiffraction patterns contain additional extra reflections of the $1/5\langle 220 \rangle^*L_{21}$ type and $1/7\langle 220 \rangle^*L_{21}$ (Figures 11 and 12).

From the above data of transmission electron microscopy, it can be seen that the intermartensitic transformation $10 M \rightarrow 14 M$ practically does not lead to a change in the crystallographic orientation of the martensitic regions. The electron diffraction patterns obtained from 5 M and 7 M martensites (Figures 10b and 12b) show only a change in the long-period modulation of the stacking of the basal planes. Therefore, these intermartensitic transformations may not be reflected in the measurements of physical properties and can be manifested only using the TEM method, which makes it interesting to study the evolution of modulated structures near the intermartensitic transition.

As mentioned above [9–17], the properties of Ni-Mn-In (Ga) systems and other three, four, or more component systems are extremely dependent on the elemental composition. However, the reproducibility of the elemental composition is an extremely complex and basic task and one of the most important problems, even taking into account the large errors (0.1–1%) of the most common methods for its determination (EDX and WDX), which makes it difficult to use these alloys as structural and functional. A detailed study of the fine structure makes it possible to determine the necessary structural elements responsible for the manifestation of unique effects (MF, SME, MCE, etc.).

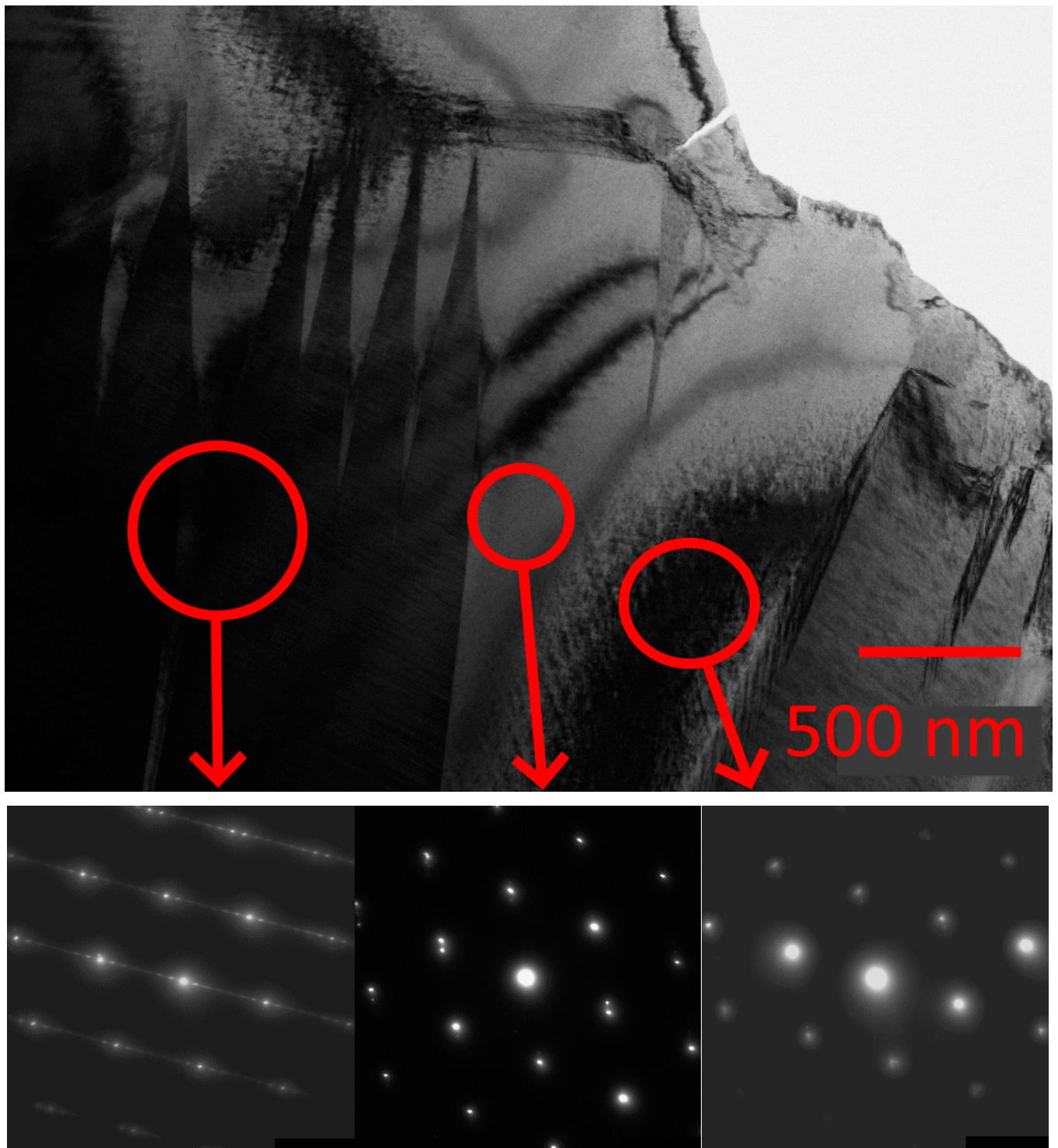
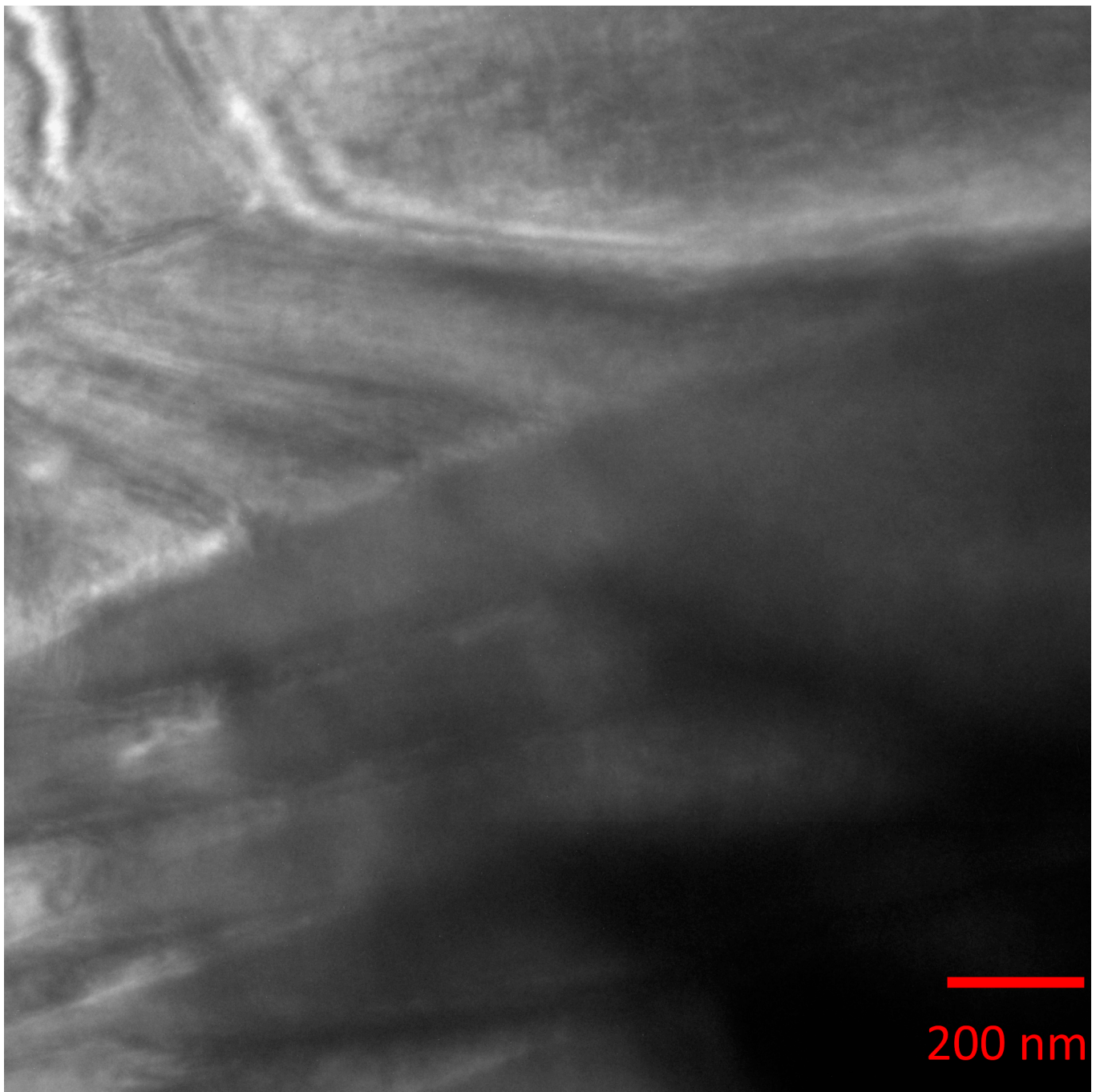
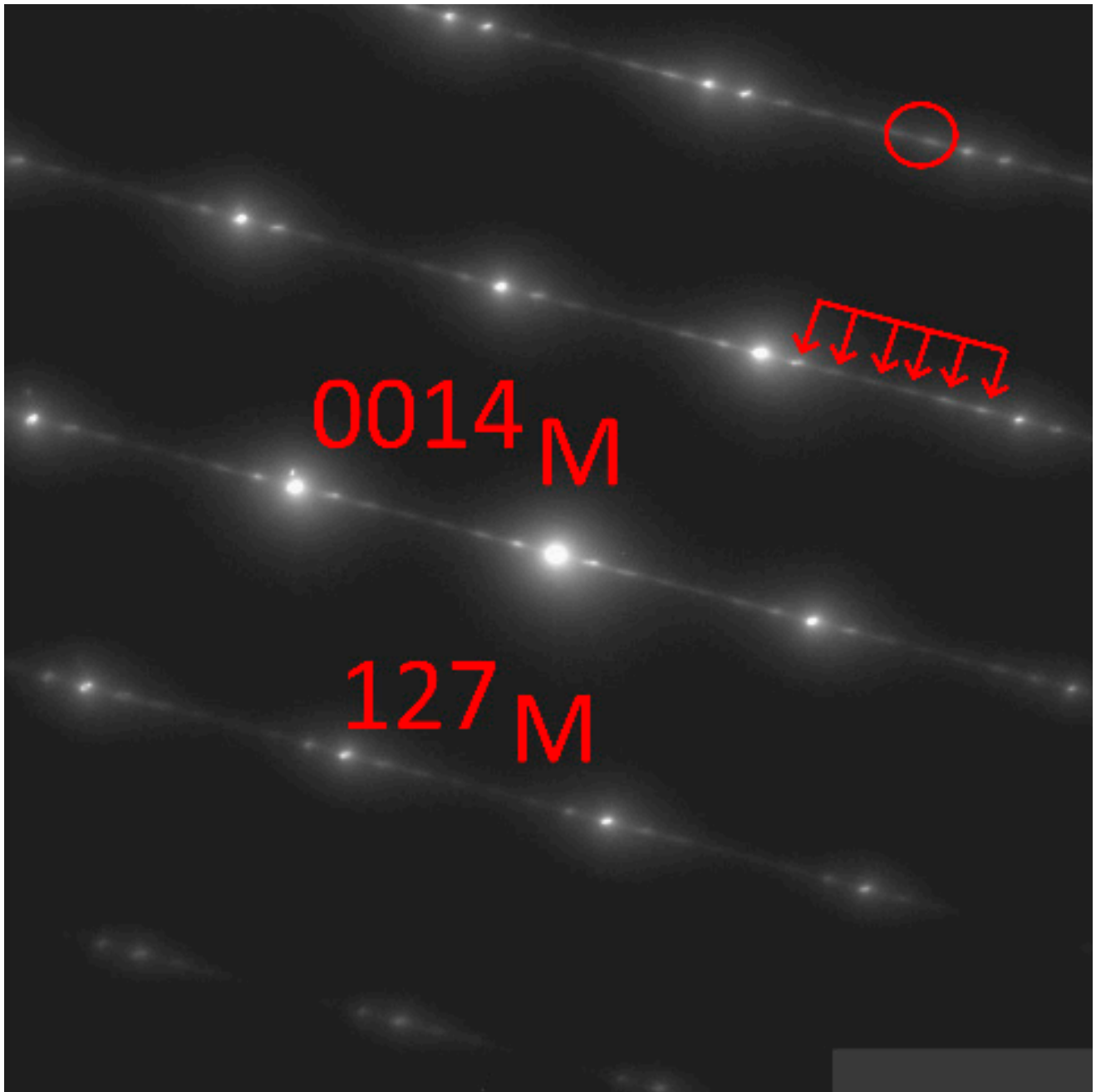


Figure 11. Bright-field image of the microstructure of a slowly cooled $\text{Ni}_{45}\text{Mn}_{40}\text{In}_{15}$ alloy obtained at 120 K and electron diffraction patterns with the $[111]L_2$ zone axis from the indicated regions.



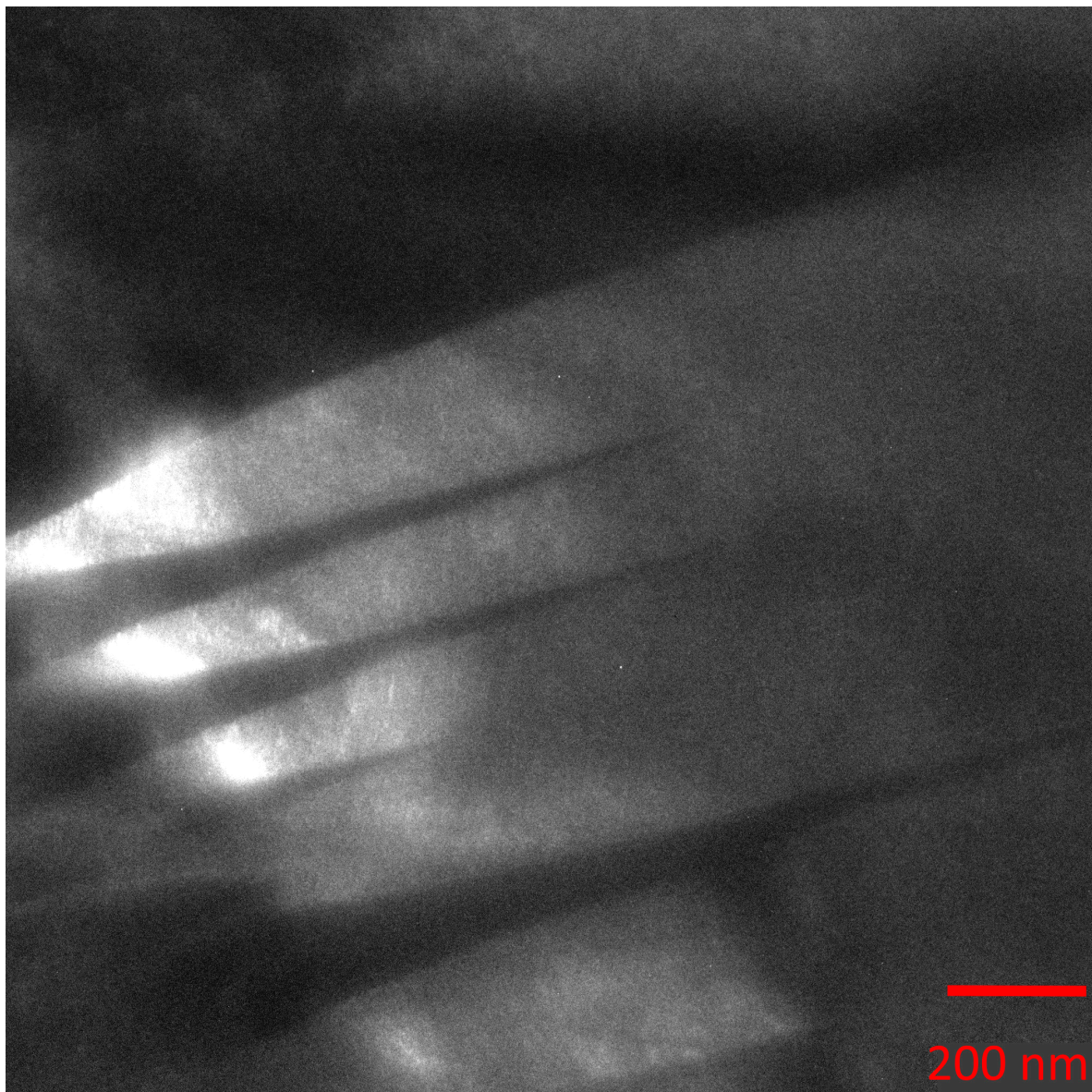
(a)

Figure 12. Cont.



(b)

Figure 12. Cont.



(c)

Figure 12. Bright-field TEM image (a), with the corresponding microelectron diffraction pattern with the $[111]L_{21}$ zone axis, (b) and dark-field TEM image in the extra reflections marked with a circle in the electron diffraction pattern (c) of the slowly cooled $Ni_{45}Mn_{40}In_{15}$ alloy. Observations at 120 K.

4. Conclusions

The research findings indicate that quenching from a temperature exceeding the $B2 \rightarrow L_{21}$ ordering temperature augments the latent heat of martensitic transformation compared to a slowly cooled alloy, thereby potentially enhancing the MCE value. The cooling rate was found to influence both the Curie temperature (lower for a quenched alloy than a slowly cooled one) and the temperatures of the direct and reverse martensitic transformation. However, the hysteresis width remains virtually unchanged for the heat treatments examined. Post-quenching and slow cooling, the austenite's fine structure in the non-stoichiometric Ni-Mn-In alloy comprises a blend of solid solutions ($B2 + L_{21}$) in varying proportions. The primary diffraction spots are effectively indexed by a cubic cell with a lattice parameter $a = 5.99 \text{ \AA}$ for L_{21} . Both alloys undergo a martensitic transformation from austenite to 10 M and 14 M modulated structures. Accelerating the cooling rate of Ni-Mn-In system alloys (with $In \ 10 < x \leq 16\%$) from a temperature above the $B2 \rightarrow L_{21}$

ordering temperature results in the suppression of austenite solid solution decomposition and a consequent increase in APB density. The quenched alloy remained in the austenite–martensitic (L21/B2 + 10 M or 14 M) state up to a temperature of 120 K. More comprehensive atomic ordering of the structure according to the L21 type in a slowly cooled alloy led to a decrease in APB density and the emergence of a transition temperature range (150–120 K) with a two-step transformation L21/B2 → 10 M → 14 M.

Author Contributions: Conceptualization, D.K.; Methodology, E.K. and D.D.; Validation, S.v.G.; Formal analysis, E.K. and A.M.; Investigation, A.M., D.D., G.S., I.M., I.S., A.P., S.v.G. and V.S.; Resources, G.S.; Writing—original draft, D.K.; Writing—review & editing, D.K. and E.K.; Supervision, V.S. All authors have read and agreed to the published version of the manuscript.

Funding: Thermal analysis (DSC, TMA, TGA) and X-ray diffraction experiments were supported by the Russian Science Foundation, grant no. 20-19-00745, <https://rscf.ru/project/23-19-45040/> (accessed on 1 January 2023). The investigation of the structure by means of SEM/TEM/electron microscopy was carried out at the IRC for Nanotechnology of the Science Park of St. Petersburg State University within the framework of project no. AAAA-A19-119091190094. The interpretation and analysis of X-ray diffraction and electron microscopy data were carried out in the framework of the state task by the Russian Ministry of Education and Science (topic “Pressure” No. 122021000032-5), M.N. Mikheev Institute of Physics of Metals, Ural Branch of the Russian Academy of Sciences.

Data Availability Statement: The data presented in this study are available on request from the corresponding author.

Acknowledgments: The authors express their gratitude to Vladimir Vasilievich Khavaylo, MISiS University of Science and Technology, for assistance in organizing the experiment.

Conflicts of Interest: The authors declare no conflict of interest.

References

1. Yang, Z.; Cong, D.Y.; Huang, L.; Nie, Z.H.; Sun, X.M.; Zhang, Q.H.; Wang, Y.D. Large Elastocaloric Effect in a Ni-Co-Mn-Sn Magnetic Shape Memory alloy. *Mater. Des.* **2016**, *92*, 932–936. [\[CrossRef\]](#)
2. Krenke, T.; Acet, M.; Wassermann, E.F.; Moya, X.; Mañosa, L.; Planes, A. Ferromagnetism in the austenitic and martensitic states of Ni–Mn–In alloys. *Phys. Rev. B* **2006**, *73*, 174413–174414. [\[CrossRef\]](#)
3. Liu, Z.H.; Li, G.T.; Wu, Z.G.; Ma, X.Q.; Liu, Y.; Wu, G.H. Tailoring martensitic transformation and martensite structure of NiMnIn alloy by Ga doping. *J. Alloys Compd.* **2012**, *535*, 120–123. [\[CrossRef\]](#)
4. Kojima, T.; Kameoka, S.; Tsai, A.P. The emergence of Heusler alloy catalysts. *Sci. Technol. Adv. Mater.* **2019**, *20*, 445–455. [\[CrossRef\]](#)
5. Kuznetsov, D.D.; Kuznetsova, E.I.; Mashirov, A.V.; Loshachenko, A.S.; Danilov, D.V.; Mitsiuk, V.I.; Kuznetsov, A.S.; Shavrov, V.G.; Koledov, V.V.; Ari-Gur, P. Magnetocaloric Effect, Structure, Spinodal Decomposition and Phase Transformations Heusler Alloy Ni-Mn-In. *Nanomaterials* **2023**, *13*, 1385. [\[CrossRef\]](#) [\[PubMed\]](#)
6. Eleno, L.T.F.; Errico, L.A.; Gonzales-Ormeño, P.G.; Petrilli, H.M.; Schön, C.G. Ordering phase relationships in ternary iron aluminides. *Calphad* **2014**, *44*, 70–80. [\[CrossRef\]](#)
7. Murakami, Y.; Yanagisawa, K.; Niitsu, K.; Park, H.S.; Matsuda, T.; Kainuma, R.; Shindo, D.; Tonomura, A. Determination of magnetic flux density at the nanometer-scale antiphase boundary in Heusler alloy Ni₅₀Mn₂₅Al_{12.5}Ga_{12.5}. *Acta Mater.* **2013**, *61*, 2095–2101. [\[CrossRef\]](#)
8. Vronka, M.; Straka, L.; De Graef, M.; Heczko, O. Antiphase Boundaries, Magnetic Domains, and Magnetic Vortices in Ni-Mn-Ga Single Crystals. *Acta Mater.* **2020**, *184*, 179–186. [\[CrossRef\]](#)
9. Rodriguez-Vargas, B.R.; Stornelli, G.; Folgarait, P.; Ridolfi, M.R.; Miranda Pérez, A.F.; Di Schino, A. Recent advances in additive manufacturing of soft magnetic materials: A review. *Materials* **2023**, *16*, 5610. [\[CrossRef\]](#)
10. Yan, H.L.; Huang, X.M.; Esling, C. Recent Progress in Crystallographic Characterization, Magnetoresponse and Elastocaloric Effects of Ni-Mn-In-Based Heusler Alloys—A Review. *Front. Mater.* **2022**, *9*, 85. [\[CrossRef\]](#)
11. Xu, N.; Raulot, J.M.; Li, Z.B.; Bai, J.; Yang, B.; Zhang, Y.D.; Meng, X.Y.; Zhao, X.; Zuo, L.; Esling, C. Composition-dependent structural and magnetic properties of Ni–Mn–Ga alloys studied by ab initio calculations. *J. Mater. Sci.* **2015**, *50*, 3825–3834. [\[CrossRef\]](#)
12. Jin, X.; Marioni, M.; Bono, D.; Allen, S.M.; O’handley, R.C.; Hsu, T.Y. Empirical mapping of Ni–Mn–Ga properties with composition and valence electron concentration. *J. Appl. Phys.* **2002**, *91*, 8222–8224. [\[CrossRef\]](#)
13. Wu, S.K.; Yang, S.T. Effect of composition on transformation temperatures of Ni–Mn–Ga shape memory alloys. *Mater. Lett.* **2003**, *57*, 4291–4296. [\[CrossRef\]](#)
14. Sakon, T.; Adachi, Y.; Kanomata, T. Magneto-structural properties of Ni₂MnGa ferromagnetic shape memory alloy in magnetic fields. *Metals* **2013**, *3*, 202–224. [\[CrossRef\]](#)

15. Wisz, G.; Sagan, P.; Stefaniuk, I.; Cieniek, B.; Maziarz, W.; Kuzma, M. Structure and composition of layers of Ni-Co-Mn-In Heusler alloys obtained by pulsed laser deposition. *EPJ Web Conf. EDP Sci.* **2017**, *133*, 02006. [[CrossRef](#)]
16. Kamal, S.K.; Vimala, J.; Sahoo, P.K.; Durai, L. Chemical Characterisation of Bulk and Melt-spun Ribbons of NiMnIn Alloy using Inductively Coupled Plasma Optical Emission Spectrometry. *Def. Sci. J.* **2011**, *61*, 270. [[CrossRef](#)]
17. Pushin, V.; Kuranova, N.; Marchenkova, E.; Pushin, A. Design and development of Ti-Ni, Ni-Mn-Ga and Cu-Al-Ni-based alloys with high and low temperature shape memory effects. *Materials* **2019**, *12*, 2616. [[CrossRef](#)]
18. Zhang, X.; Zhang, H.; Qian, M.; Geng, L. Enhanced magnetocaloric effect in Ni-Mn-Sn-Co alloys with two successive magnetocrystallographic transformations. *Sci. Rep.* **2018**, *8*, 8235. [[CrossRef](#)]
19. Kaletina, Y.V.; Frolova, N.Y.; Gundyrev, V.M.; Kaletin, A.Y. Phase Transformations and Structure of Ni-Mn-In Alloys with Varying Ratio Ni/Mn. *Phys. Solid State* **2016**, *58*, 1663–1670. [[CrossRef](#)]
20. Kaletina, Y.V.; Kabanova, I.G.E.; Frolova, N.Y.; Gundyrev, V.M.; Kaletin, A.Y. Crystallographic Specific Features of the Martensitic Structure of Ni₄₇Mn₄₂In₁₁ Alloy. *Phys. Solid State* **2017**, *59*, 2008–2015. [[CrossRef](#)]
21. Kuznetsov, D.D.; Kuznetsova, E.I.; Mashirov, A.V.; Loshachenko, A.S.; Danilov, D.V.; Shandryuk, G.A.; Shavrov, V.G.; Koledov, V.V. In Situ TEM Study of Phase Transformations in Nonstoichiometric Ni₄₆Mn₄₁In₁₃ Heusler Alloy. *Phys. Solid State* **2022**, *64*, 15–21. [[CrossRef](#)]

Disclaimer/Publisher's Note: The statements, opinions and data contained in all publications are solely those of the individual author(s) and contributor(s) and not of MDPI and/or the editor(s). MDPI and/or the editor(s) disclaim responsibility for any injury to people or property resulting from any ideas, methods, instructions or products referred to in the content.